

Journal of Nuclear Science and Technology



ISSN: (Print) (Online) Journal homepage: www.tandfonline.com/journals/tnst20

Connection of four-dimensional Langevin model and Hauser-Feshbach theory to describe statistical decay of fission fragments

Kazuki Fujio, Shin Okumura, Chikako Ishizuka, Satoshi Chiba & Tatsuya Katabuchi

To cite this article: Kazuki Fujio, Shin Okumura, Chikako Ishizuka, Satoshi Chiba & Tatsuya Katabuchi (2024) Connection of four-dimensional Langevin model and Hauser-Feshbach theory to describe statistical decay of fission fragments, Journal of Nuclear Science and Technology, 61:1, 84-97, DOI: 10.1080/00223131.2023.2273470

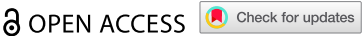
To link to this article: https://doi.org/10.1080/00223131.2023.2273470

9	© 2024 The Author(s). Published by Informa UK Limited, trading as Taylor & Francis Group.
	Published online: 30 Nov 2023.
	Submit your article to this journal 🗷
ılıl	Article views: 536
Q	View related articles 🗹
CrossMark	View Crossmark data 🗹
4	Citing articles: 2 View citing articles 🗹









Connection of four-dimensional Langevin model and Hauser-Feshbach theory to describe statistical decay of fission fragments

Kazuki Fujio 📭, Shin Okumura 📭, Chikako Ishizuka 📭, Satoshi Chiba 📭 dand Tatsuya Katabuchi 📭

^aNuclear Engineering Course, Department of Transdisciplinary Science and Technology, School of Environment and Society, Tokyo Institute of Technology, Tokyo, Japan; bNAPC-Nuclear Data Section, International Atomic Energy Agency, Vienna International Centre, Vienna, Austria; Institute of Innovative Research, Tokyo Institute of Technology, Tokyo, Japan; MAT Research Center, NAT Corporation, Ibaraki, Japan

ABSTRACT

We have developed a novel theoretical method to obtain independent fission product yields and prompt neutron observables by connecting mass and total kinetic energy (TKE) distributions calculated by a four-dimensional Langevin dynamical model to a Hauser-Feshbach statistical decay model. In the Langevin calculations, mass distributions corresponding to the standard I and II modes were obtained separately and superposed to reproduce the fission fragment yield of spontaneous fission of ^{238,240,242}Pu and thermal neutron-induced fission of ²³⁹Pu. This was achieved by using different neck parameters for these two modes in the twocenter shell model shape parametrization, and a systematics of the superposing ratio was obtained as a function of (N-Z)/A of the fissioning nuclei. The Hauser-Feshbach calculations were performed using a nuclear reaction code TALYS for 239 Pu(n, f) reaction in the incident energy range from thermal up to 5 MeV, and the calculated prompt fission observables were compared with experimental and evaluated data. Although further improvements are needed for the most important nuclides, it turned out that the present methodology has the capability to prepare fission-related nuclear data for nuclides for which measurements are difficult.

ARTICLE HISTORY

Received 27 June 2023 Accepted 12 October 2023

KEYWORDS

Nuclear fission; Langevin model: Hauser-Feshbach statistical decay: Fission yield; Prompt fission

1. Introduction

Accurate evaluation of fission observables is essential for accurate design of nuclear reactors and for nuclear transmutation technology such as accelerator-driven systems [1]. In particular, the mass distribution of fission products (after prompt neutron emission) and emitted neutrons from fission fragments (before prompt neutron emission) have been studied in detail experimentally and theoretically. The independent fission product yield, namely, the isotopic distribution of fission products after prompt particle emissions, determines the total amount of radioactive waste in spent nuclear fuel and affects disposal scenarios of radioactive waste [2]. The prompt neutron multiplicity, that is, the average number of emitted prompt neutrons, is important for evaluating the criticality of nuclear reactors, and the prompt fission neutron spectrum (PFNS) is also essential for criticality and analysis of burn-up characteristics [3]. For each fission observable, there are several theoretical efforts relying on empirical models [4-6] and models based on nuclear physics [7], respectively. Currently, approaches using Monte Carlo samplings, such as CGMF [8,9], FIFRELIN [10], FREYA [11,12], and GEF [13], or deterministic approaches,

such as DSE [14], HF³D [15], PbP [16], and TALYS [17] have been developed to evaluate fission observables in a consistent manner since they are mutually correlated.

The fission reaction is a dynamical process caused by nuclear deformation and can be described by several different steps. In the case of neutron-induced fission, an excited compound nucleus undergoes shape deformation by a collective motion of its internal nucleons. After surmounting multiple fission barriers, the compound nucleus forms a narrow neck. The compound nucleus is divided into two highly excited fission fragments by the scission of the neck, and more than a thousand types of fragments are produced stochastically. After scission, the fission fragments proceed to the prompt decay process to release their excitation energy. In the prompt decay process, the fragments are de-excited to their ground states or the isomeric states by emitting prompt neutrons and γ rays. Then β^- decay takes place in neutron-rich independent fission products towards the final stable or long-lived cumulative fission products.

As described above, nuclear fission starts with nuclear deformation and involves several complex physical processes which include the prompt decay and β^{-} decay processes. Since the fission process consists of several different physical mechanisms, it is necessary to combine multiple theories to describe the entire process. For the process up to scission, approaches describing the potential energy of a compound nucleus have been developed by using microscopic models [18-23] and macro-microscopic models [24-32]. The Langevin approach is one of the methods that can describe part of the fission process by using the macro-microscopic potential [24,26,28,29]. The Langevin equation is a stochastic differential equation of motion that describes Brownian motion of collective variables in a heat bath formed by nucleons, taking into account effects of a random force acting on macroscopic coordinates. In nuclear physics, the Langevin model simulates the fission process from nuclear deformation after forming a compound nucleus up to scission. In our four-dimensional Langevin model, we have succeeded in understanding mode transitions of the fission fragment yield and total kinetic energy (TKE) distribution over a wide mass range from actinide to superheavy nuclei [29,33,34]. However, we need more precise data for the width and peak positions of the mass distribution for nuclear applications than our previous approach.

In this work, we have developed a new method to evaluate the prompt fission observables by connecting the four-dimensional Langevin model and the Hauser-Feshbach statistical decay model. This comprehensive approach enables the consistent calculation of the prompt fission observables based on nuclear physics. The fission fragment yields corresponding to the standard I and II modes are calculated separately in the Langevin model and are superposed to reproduce the fission fragment yield of spontaneous fission of $^{238,240,242}Pu\overset{(238,240,242}{(238,240,242}Pu(sf))} \ \ and \ \ thermal \ \ neutron$ induced fission of 239 Pu (239 Pu(n_{th}, f)).

The obtained fission fragment yield and total kinetic energy (TKE) are employed as input for the Hauser-Feshbach statistical decay calculations in TALYS. The prompt fission observables of ²³⁹Pu(n, f) are compared with reported data at incident energies from thermal up to 5 MeV. We show a systematics of the superposing ratio in the fission fragment yield and discuss the reproduced trends and discrepancies in the calculation results.

In Section 2, we introduce the four-dimensional Langevin model, our approach by superposing two different fission modes, and how we prepare the input for the Hauser-Feshbach statistical decay calculations. In Section 3, we show the fission fragment yields and TKEs obtained from the four-dimensional Langevin model and the prompt fission observables calculated in TALYS using the Langevin fission fragment data. Conclusions are given in Section 4.

2. Models and calculation method

2.1. Four-dimensional Langevin model

We employed the four-dimensional Langevin model [29,33,34] for simulating the deformation of a compound nucleus up to scission. The time evolution of nuclear deformation is solved in the Langevin equation on the corresponding free energy with transport coefficients:

$$\frac{dq_{\mu}}{dt} = (m^{-1})_{\mu\nu} p_{\nu},$$

$$\frac{dp_{\mu}}{dt} = -\frac{\partial F(q, T)}{\partial q_{\mu}} - \frac{1}{2} \frac{\partial (m^{-1})_{\nu\sigma}}{\partial q_{\mu}} p_{\nu} p_{\sigma}$$

$$-\gamma_{\mu\nu} (m^{-1})_{\nu\sigma} p_{\sigma} + \sqrt{T_{\mu}^{eff}} g_{\mu\nu} R_{\nu}(t), \quad (1)$$

where $\{q_{\mu}: \mu=1\cdots 4\}$ is a set of collective variables of nuclear shape, and $\{p_{\mu}\}$ is the corresponding conjugate momenta. We do not take the sum on μ in the last term of the second equation. The symbol R_{ν} represents a stochastic force having a white-noise nature.

The time-dependent collective $\{q_{\mu}\}=\{z_0/R_0,\delta_1,\delta_2,\alpha\}$ and a neck parameter ε are represented in the two-center shell model (TCSM) [35]. Figure 1 shows a schematic potential of the TCSM and the nuclear shape as a function of an axis for nuclear elongation. The first variable z_0/R_0 represents nuclear elongation normalized by the radius of the compound nucleus $R_0 = 1.2A^{1/3}$, where A is the mass number of the compound nucleus. The second and third variables δ_i (i = 1, 2) correspond to the deformations of the outer tip of each right and left fragment. The fourth variable α denotes the mass asymmetry calculated as the relative difference of mass numbers of each fragment. The neck configuration is described by a parameter ε using the ratio of the intercept of two harmonic oscillators of the TCSM and that of a connecting function ($\varepsilon = E/E_0$), where E_0 is the actual barrier height. The parameter ε affects the peak positions of the fission fragment yield and overall TKE. A large ε value results in a thin neck, forming fragments with a compact Consequently, the peak position shifts towards A = 134 due to the double magicity in heavy fragments. Given that Coulomb energy significantly influences TKE, changes in ε also affect TKE. A large ε reduces the distance between fragments, leading to a high Coulomb energy. As a result, TKE increases.

The free energy F(q, T) in Equation (1) is temperature-dependent and is calculated F = V - TS, where V is the nuclear potential energy, T is the nuclear temperature, and S is the entropy. We employed F(q, T) instead of the potential energy to accurately calculate the

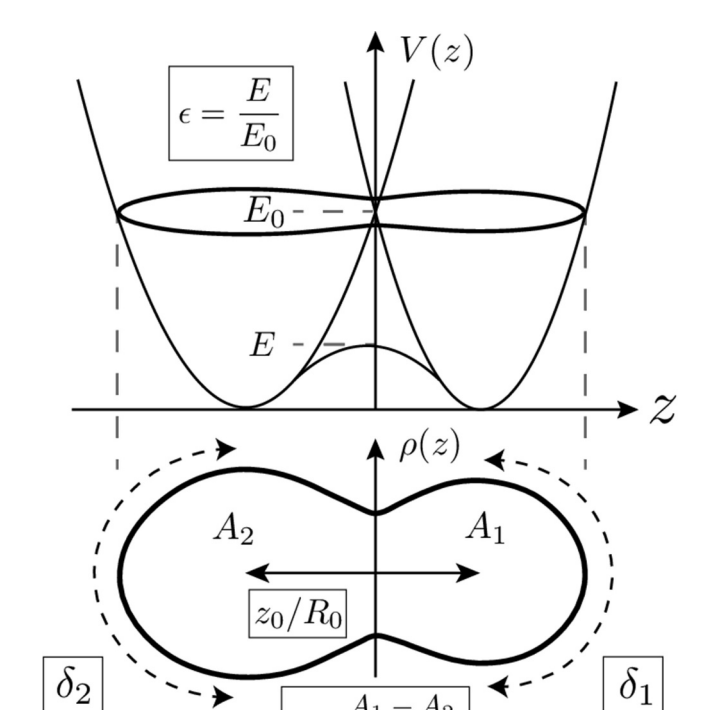


Figure 1. The potential of the two-center shell model and the nuclear shape.

temperature dependence of the shell correction. The shell and pairing corrections to the free energy were determined in our previous work by a temperature-dependent calculation [36]. The single-particle energy is calculated in the finite-depth two-center Woods-Saxon potential with parameters from Ref [37], and the TCSM shape was expanded by Cassini ovaloids. Regarding transport coefficients, we calculated a collective inertia tensor $m_{\mu\nu}$ under Werner-Wheeler approximation [38,39]. For a friction tensor $\gamma_{\mu\nu}$, we applied wall-andwindow formula with a commonly accepted reduction factor $k_s = 0.27$ [40-42]. As for the random force, the strength $g_{\mu\nu}$ of the random force connects to the friction tensor through the fluctuationdissipation theorem at 1 MeV:

$$g_{\mu\sigma}g_{\sigma\nu} = \gamma_{\mu\nu}.\tag{2}$$

The intrinsic temperature of the system T governs the strength of the shell effect, and T is connected to the intrinsic excitation energy E_{int} with the level density parameter a:

$$E_{\rm int} = E_x - \frac{1}{2} \left(m^{-1} \right)_{\mu\nu} p_{\mu} p_{\nu} - F(q, T = 0) = a T^2, \tag{3}$$

where E_x is the input excitation energy and is treated as the sum of the neutron separation energy and the incident energy. In our model, the effective temperature T_{μ}^{eff} is introduced for collective variables as below:

$$T_{\mu}^{\text{eff}} = \frac{1}{2}\hbar\omega_{\mu} \coth\frac{\hbar\omega_{\mu}}{2T},\tag{4}$$

where ω_{μ} is the local frequency of collective motion. At T=0, $T_{\mu}^{\rm eff}$ corresponds to the zero-point energy $\hbar\omega_{\mu}/2$, i.e., $T_{\mu}^{\rm eff}=\hbar\omega_{\mu}/2$. A larger value of $\hbar\omega_{4}$ gives a wider width of the fission fragment yield and higher average TKE around A=120-130. For the value of parameters ε and $\hbar\omega_{\mu}$ in this research, refer to Section 2.2.

In a recent microscopic approach, it is concluded that the collective motion is overdamped, so the inertia is irrelevant [21,22]. In the Langevin approach, however, we describe the collective motion in a different context. We start the calculation from a point close to the ground state, and the fluctuations lead the trajectories to pass over the saddle point so that we can obtain distributions of physical quantities, such as mass and TKE. We need the terms containing the inertia tensor so that our approach to be self-consistent to describe all these processes consistently. We hope that the relation between these two different views on the collective motion should be elucidated well in the future.

2.2. Superposition of two different fission modes

In our previous calculations, the width and peak positions of the mass distribution were not well reproduced because the model restricts to one neck parameter ε [43]. The neck parameter ε is a fixed

parameter in the four-dimensional Langevin model due to the limitations of calculation time and resources. However, in the original concept of the TCSM, ε is also supposed to be one of the dynamic variables, and a distribution of ε should exist at the scission point. From the previous findings, it is known that the fission yields can be expressed in the superposition of several different fission modes. The fission modes are determined by the peak positions of the fission fragment yield, and the TKE and the peak positions differ accordingly in these modes. To incorporate different fission modes in our Langevin model, we superposed two Langevin calculations. The classification of fission modes was inspired by Brosa's notation [44], and this approach enabled us to express the variations in ε in the fission fragment yield and TKE.

Brosa et al. suggested a model on different fission paths: the superlong (SL), supershort (SS), standard I (ST1), and standard II (ST2) modes [44]. The SL and SS modes represent symmetric fission components and are distinguished by the nuclear shape. The SL mode gives smaller TKE due to the large deformation of fission fragments, whereas the SS mode produces larger TKE owing to the compact shape of fragments. The ST1 and ST2 modes are asymmetric fission components and are classified by the peak positions. For heavy fragments, the peak position of ST1 mode is located near A = 134 due to the doubly magic shell, and its nuclear shape shows a spherical configuration in the ground state. The peak position of ST2 mode is in the vicinity of A = 144 due to the deformed shell, and the shape exhibits deformed. By using this classification, we developed a phenomenological approach to describe the fission fragment mass yield systematically over a wide mass range.

Currently, few fissile isotopes exist in experimental and evaluated data for the fission observables before and after prompt decay. The fission fragment yields are reported for $^{238,240,242}Pu(sf)$ and $^{239}Pu(n_{th},f)$ from Ref [45]. For this reason, we decomposed the experimental fission fragment yields of ²⁴⁰Pu(sf) into two fission fragment yields corresponding to the ST1 and ST2 modes and calculated two modes separately by changing ε and $\hbar\omega_{\mu}$ parameters in our Langevin model. As indicated in Section 2.1, the peak positions of the fission fragment yield and overall TKE are highly influenced by the parameter ε , and the width of the yield and TKE ranging of A = 120 - 130 are notably sensitive to the parameter $\hbar\omega_4$. The parameters are determined to be $\varepsilon=0.65$ and $\hbar\omega_{\mu}=(2,2,2,1)$ MeV for the ST1 mode and to be $\varepsilon = 0.25$ and $\hbar \omega_{\mu} = (2, 2, 2, 2.7)$ MeV for the ST2 mode. The neck parameter ε differs between the ST1 and ST2 modes because ε reflects the characteristics of nuclear shape, and we confirmed the ST1 mode as a spherical shape and the ST2 mode as a deformed shape at peak positions in heavy fragments. The width

of the fission fragment yield tends to be smaller for the ST1 mode than for the ST2 mode in the actinide nuclides. The symmetric components are included in the ST2 mode in our Langevin calculations; therefore, we did not superpose the SL and SS modes separately and applied a damping function to the symmetric components of the SL mode at thermal energy. It must be noted the SL mode is associated with the ST2 mode since fragments in both modes are deformed. We summed up the calculated ST1 and ST2 modes using a superposing ratio ζ :

$$Y_{\rm ff}(A,{\rm TKE}) = \zeta Y_{\rm ST1}(A,{\rm TKE}) \\ + (1-\zeta)Y_{\rm ST2}(A,{\rm TKE}), \qquad (5)$$

where $Y_{ST1}(A, TKE)$ and $Y_{ST2}(A, TKE)$ are fission fragment yields of ST1 and ST2 modes. The same ε and $\hbar\omega_{\mu}$ sets are used for $^{238,240,242}Pu(sf)$ and $^{239}Pu(n,f)\text{,}$ and we only adjusted ζ by using a least squares method to reproduce the peak positions of fission fragment yields.

2.3. Connection to the Hauser-Feshbach statistical decay calculations

We calculated the prompt decay process with the Hauser-Feshbach theory implemented in TALYS (version:1.96) [17] using the fission fragment yields $Y_{\rm ff}(A)$ and average TKE ($\langle TKE \rangle (A)$) from our Langevin model. The necessary information for the prompt decay calculation is not only $Y_{\rm ff}(A)$ and $\langle TKE \rangle (A)$ but also the charge distribution of mass distribution and TKE, the excitation energy distribution, and the spin-parity distribution of fission fragments. For the charge distribution, we employed Wahl's Z_p model [4,5] for each fragment obtained from the Langevin calculations. The average total excitation energy and its dispersion for each fragment pair are calculated with the Q-value, $\langle TKE \rangle$, and its dispersion from the Langevin model. The average excitation energy is distributed into each fission fragment based on an anisothermal parameter R_T [15,46–49]; defined as a ratio of nuclear temperatures $T_{l,h}$ of light and heavy fission fragments:

$$R_T = \frac{T_l}{T_h} = \sqrt{\frac{U_l a_h(U_h)}{U_h a_l(U_l)}},\tag{6}$$

where $a(U_{l,h})$ are the level density parameters, and $U_{l,h}$ are the excitation energies corrected by the pairing energies. The energy dependence of R_T is introduced as in the previous research [49]:

$$R_T = \begin{cases} R_{T_0} + E_n R_{T_1}, & R_{T_0} + E_n R_{T_1} \ge 1, \\ 1, & \text{otherwise,} \end{cases}$$
 (7)

where R_{T_0} and R_{T_1} are model parameters, and we used $\ensuremath{\ensuremath{R_{T_0}}} = 1.30$ and $\ensuremath{\ensuremath{R_{T_1}}} = -0.507$ for the $^{239}Pu(n,f)$

The excitation energy and spin-parity distributions are calculated in TALYS. TALYS generates the excitation energy distribution of each fission fragment in the form of a Gaussian distribution by using the average excitation energy and its dispersion. The energy and its dispersion are prepared with the calculated Langevin results and the energy-dependent R_T value. The spin-parity distribution is provided in the form of Fermi-gas model. The parameters in the spin-parity distribution are selected to reproduce the neutron multiplicity at thermal incident energy. For further details, please refer to the relevant reference [50].

3. Results and discussion

3.1. Fission fragment yield and average TKE obtained from four-dimensional Langevin model

We calculated the fission fragment yields $Y_{\rm ff}(A)$ and average TKEs $(\langle TKE \rangle (A))$ of both ST1 and ST2 modes separately in the Langevin model and superposed them by using a superposing ratio ζ . The upper part of Figure 2 shows $Y_{\rm ff}(A)$, and the lower part of Figure 2 represents $\langle TKE \rangle (A)$ for ^{238,240,242}Pu(sf). By adjusting ζ , the peak position of $Y_{\rm ff}(A)$ is successfully reproduced for 238,240,242 Pu(sf). The calculated $\langle TKE \rangle (A)$ is also in agreement with experimental data. The results represent that the TKE of the ST1 mode is higher than that of the ST2 mode. TKE is calculated as the sum of Coulomb and kinetic energies at scission, as mentioned in Section 2.1. In the ST1 mode, the distance between fission fragments is small due to their spherical shape. As the distance between fragments decreases, the Coulomb energy increases, leading to a higher TKE. Consequently, the ST1 mode has a higher $\langle TKE \rangle (A)$ than the ST2 mode. Table 1 shows the calculated and experimental $\langle TKE \rangle (A)$ for Pu isotopes. The deviation between our results and the experimental data is approximately 2%, which indicates our approach can provide relatively accurate $\langle TKE \rangle$ simultaneously with $Y_{\rm ff}(A)$.

Figure 3 represents the superposing ratio ζ of the ST1 and ST2 modes as a function of (N-Z)/A of the fissioning nucleus. We can see that ζ is in proportion to (N-Z)/A for ^{238,240,242}Pu(sf). This result shows the amount of $Y_{ST1}(A)$ increases linearly as (N-Z)/Aincreases. Assuming that the slope of ζ for neutroninduced fission is the same as that for spontaneous fission of Pu isotopes, the superposing approach might have the capability to calculate $Y_{\rm ff}(A)$ and TKE for neutron-induced fission of other nuclides.

We applied the same ε and $\hbar\omega_{\mu}$ obtained as above to ²³⁹Pu(n, f) ranging from thermal up to 5 MeV, and Figure 4 represents $Y_{\rm ff}(A)$ and $\langle TKE \rangle (A)$ for ²³⁹Pu(n, f) at thermal energy and at 3 and 5 MeV of incident energies. The superposing ratio ζ is adjusted to reproduce the experimental fission fragment yield of ²³⁹Pu(n_{th} , f), and the same ζ is employed for the other incident energies. The increase of $Y_{\rm ff}(A)$ in the symmetric region with increasing incident energy is well reproduced. The peak position and the width of each fission fragment yield $Y_{\rm ff}(A)$ are generally in good agreement with the experimental data although the peak position is out by a few mass numbers and is overestimated in the vicinity of A = 137, 140, especially at thermal incident energy. Regarding $\langle TKE \rangle (A)$, it is seen that the calculation results successfully reproduce

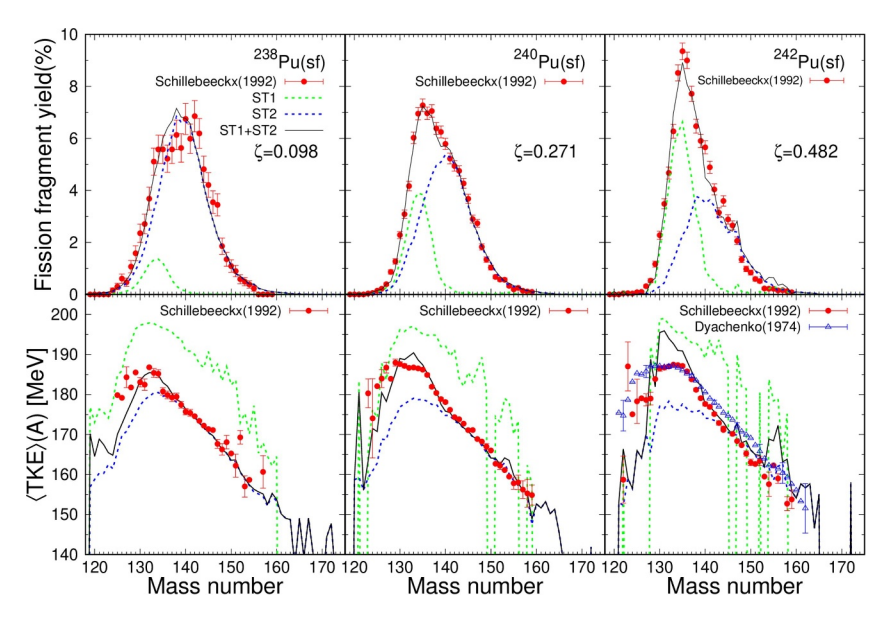


Figure 2. (Upper) the calculated fission fragment yields $Y_{\rm ff}(A)$ and (lower) the average TKEs $(\langle \textit{TKE} \rangle(A))$ for $^{238,240,242}{\rm Pu}({\rm sf})$. The green-dotted lines show the calculated ST1 modes ($\varepsilon=0.65, \hbar\omega_{\mu}=(2,2,2,1)$ MeV), the blue dotted lines represent calculated ST2 modes ($\epsilon=0.25,\hbar\omega_{\mu}=(2,2,2,2.7)$ MeV), and the black lines correspond to the superposed results of calculated ST1 and ST2 modes weighted by ζ .

 180.7 ± 0.1

	•	<i>J</i>	()	(,)
		ST1	ST2	
	ε	0.65	0.25	
	$\hbar\omega_{\mu}[{\sf MeV}]$	(2, 2, 2, 1)	(2, 2, 2, 2.7)	Average TKE
²³⁸ Pu(sf)	Present ($\zeta = 0.098$)	195.87	174.36	176.47
. ,	Demattè et al. [51]			176.4 ± 0.3
	Schillebeeckx et al. [45]			177.0 ± 0.3
²⁴⁰ Pu(sf)	Present $(\zeta = 0.271)$	194.79	173.44	179.23
` /	Demattè et al. [51]			178.5 ± 0.1
	Schillebeeckx et al. [45]			179.4 ± 0.1
$^{239}Pu(n_{th},f)$	Present ($\zeta = 0.153$)	194.78	173.65	176.88
(117)	Wagemans et al. [52,53]	192	175	
	Schillebeeckx et al. [45]			177.93 ± 0.01
	Surin et al. [54]			177.7 ± 0.1
	Tsuchiya et al. [55]			176.2 ± 1.4
²⁴² Pu(sf)	Present ($\zeta = 0.482$)	194.22	172.57	183.01
()	Demattè et al. [51]			180.5 ± 0.1

Schillebeeckx et al. [45]

Table 1. The calculated and experimental average TKE for 238,240,242 Pu(sf) and 239 Pu(n_{th}, f) in MeV unit.

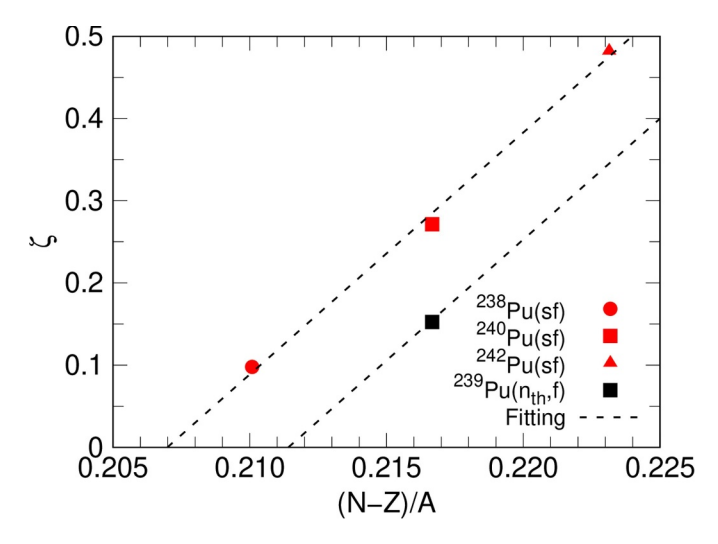


Figure 3. The superposing ratio ζ of the ST1 and ST2 modes as a function of (N-Z)/A for Pu isotopes. The dashed line represents a fitting function calculated from 238,240,242 Pu(sf).

the experimental data in $A \ge 130$ while they are underestimated around A = 120 - 130. To improve the accuracy of $\langle TKE \rangle(A)$, a large amount of fission fragment yield should be obtained from A = 120 - 130 in the ST1 mode.

Figure 5 shows $\langle TKE \rangle (E)$ as a function of incident neutron energy ranging from thermal up to 5 MeV. While the decreasing trend is reproduced in $\langle TKE \rangle (E)$ as the incident energy increases, the calculation indicates the underestimation of $\langle TKE \rangle (E)$ at thermal energy especially. One of the reasons for the underestimation in $\langle TKE \rangle (E)$ is the underestimation of $\langle TKE \rangle (A)$ in A = 120 - 130. Furthermore, there is a discrepancy between the experimental and calculated results in the slope of $\langle TKE \rangle (E)$. The previous research reported that the average TKE in Langevin calculation decreases as increasing the excitation energy due to nuclear deformation [56]. Therefore, the decreasing slope of $\langle TKE \rangle (E)$ in Langevin calculations is primarily determined by the reduction of the average TKE due to nuclear deformation. On the other hand, there are some uncertainties in the experimental TKE because the experimental TKE is obtained after

processed by theoretical or phenomenological procedures to correct the prompt decay process.

Moreover, the number of experimental TKE results is limited in actinide nuclei, and it remains incompletely understood how the average TKE decreases. We cannot conclude the reasons for the discrepancy of the decreasing slope between the calculated and experimental $\langle TKE \rangle(E)$. The investigation of TKE using the Langevin model will be conducted in the future.

3.2. Prompt fission neutron observables and independent fission product yield calculated in TALYS

By using the Hauser-Feshbach statistical decay calculations implemented in TALYS, we investigated the fission neutron observables and the independent fission product yield. Figure 6(a) shows the prompt fission neutron multiplicity $\bar{\nu}_n(A)$ for 239 Pu(n, f) as a function of mass number at the incident energies of thermal energy and 5 MeV. The calculated $\bar{\nu}_n(A)$ reproduces successfully the known tendencies, while

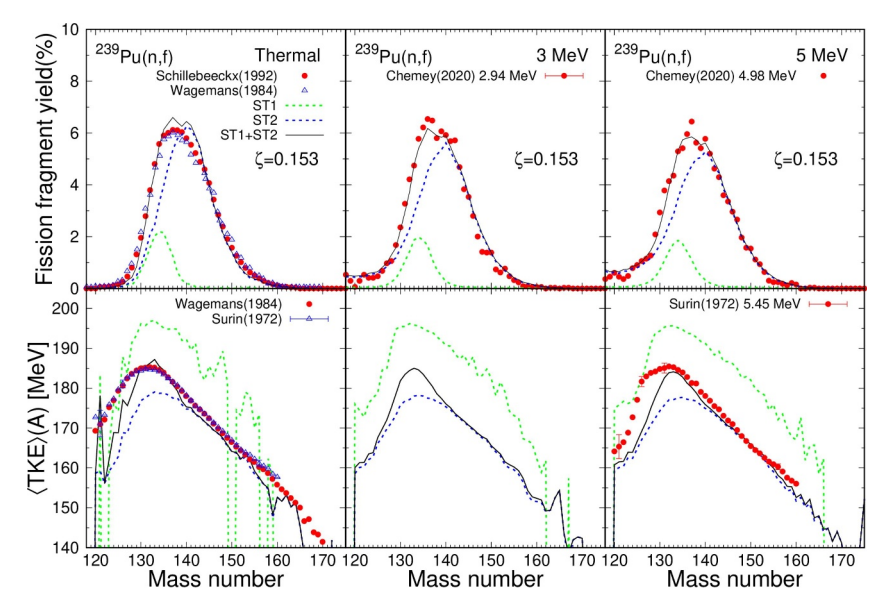


Figure 4. (Upper) the calculated fission fragment yields $Y_{\rm ff}(A)$ and (lower) the average TKEs $(\langle \textit{TKE} \rangle (A))$ for 239 Pu(n, f). The green dotted lines exhibit the calculated ST1 modes ($\varepsilon=0.65, \hbar\omega_{\mu}=(2,2,2,1)$ MeV), the blue dotted lines represent calculated ST2 modes ($\varepsilon=0.25, \hbar\omega_{\mu}=(2,2,2,2.7)$ MeV), and the black lines correspond to the superposed results of the calculated ST1 and ST2 modes weighted by $\zeta=0.153$.

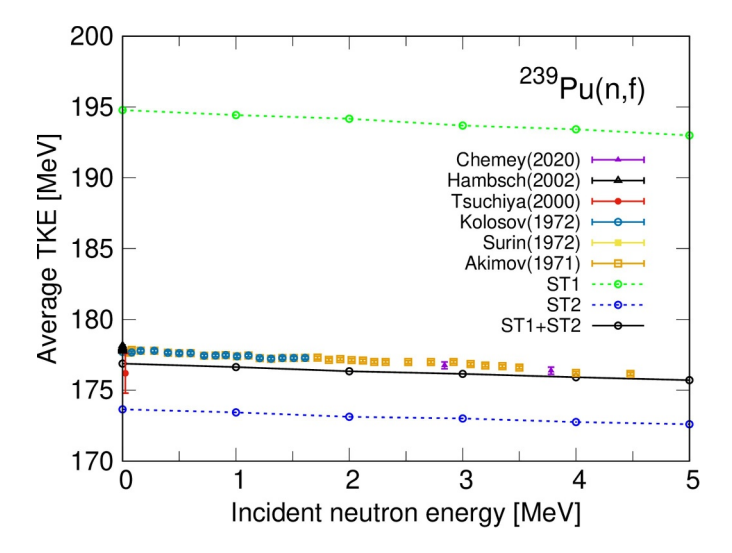


Figure 5. The average TKE $(\langle TKE \rangle(E))$ as a function of incident energy for ²³⁹Pu(n, f). The green dotted line represents the calculated ST1 mode, and the blue dotted line shows the calculated ST2 mode. The black line corresponds to the superposed result of the calculated ST1 and ST2 modes weighted by $\zeta = 0.153$.

the calculated results overestimate (underestimate) the experimental data in the light (heavy) fragments. At thermal energy, the calculated $\bar{v}_n(A)$ shows the sawtooth shape as widely known in experimental results for actinide nuclei. Compared to $\bar{v}_n(A)$ at the incident energies of thermal energy and 5 MeV, $\bar{v}_n(A)$ increases mainly from the heavy fragments owing to the energy-dependent R_T value. The trend of increasing $\bar{v}_n(A)$ from heavy fragments has been reported for several actinide nuclei in Ref [57,58]. for experimental results and several computational approaches, such as GEF, PbP [59], FIFRELIN [60], and CGMF with time-dependent superfluid local density approximation

(TDSLDA) results [21,22]. It must be noted that the saw-tooth shape and its energy dependence depend on how R_T is parameterized [61].

Figure 6(b) shows $\bar{v}_n(E)$ for 239 Pu(n,f) as a function of the incident energy ranging from thermal up to 5 MeV, and the calculated \bar{v}_n at thermal energy is tabulated with experimental and evaluated data in Table 2. The calculated $\bar{v}_n(E)$ is in fairly good agreement with experimental and evaluated data ranging from thermal up to 5 MeV even though there is a discrepancy of 1% in the calculated and experimental TKE. There are several reasons why calculated $\bar{v}_n(E)$ reproduces the reported data: (1) The discrepancy of

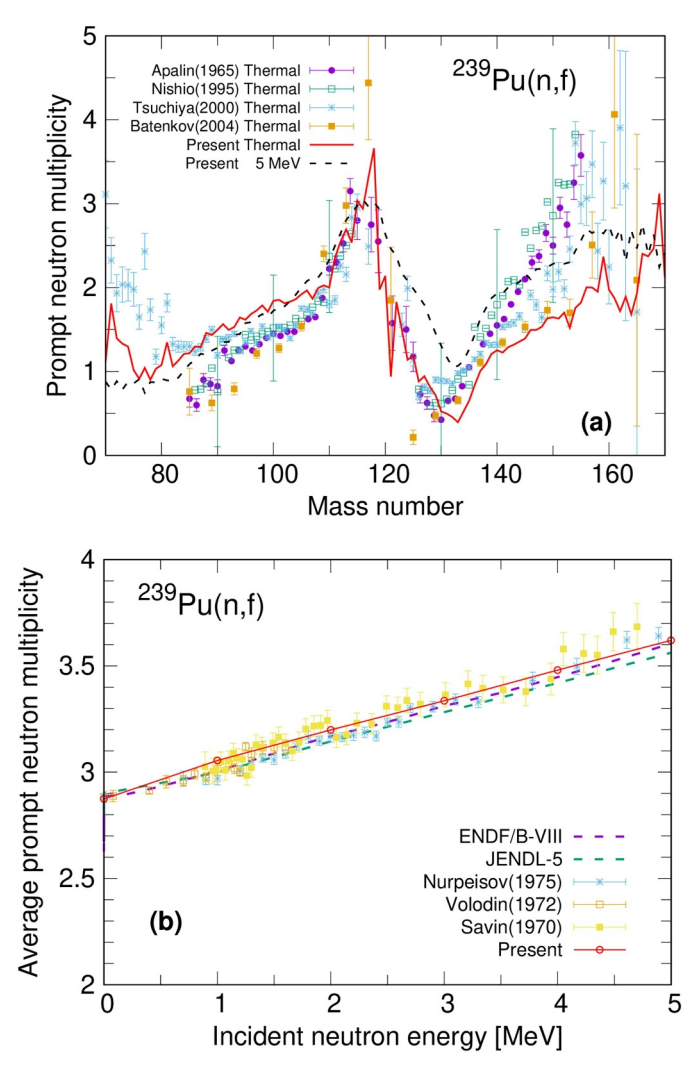


Figure 6. (a) the neutron multiplicity $\bar{v}_n(A)$ as a function of mass number at thermal and 5 MeV and (b) $\bar{v}_n(E)$ as a function of incident energy ranging from thermal up to 5 MeV for 239 Pu(n, f).

Table 2. The calculated neutron multiplicity \bar{v}_n at thermal energy for ²³⁹Pu(n, f).

	(/ /		
Present		ENDF-B/VIII.0	JENDL-5
2.874		2.870	2.870

the TKE is approximately 1 MeV, and it is small compared to the threshold energy of the prompt neutron evaporation, that is, the neutron separation energy. (2) The excitation energy affects $\bar{v}_n(E)$, and other conditions also have an influence on it, such as the spin-parity distribution of fission fragments, the fission fragment yield, and the R_T value. Various conditions overlapped, and the calculated result is in good agreement with the known data. (3) In our calculation, the overestimation and underestimation in $\bar{v}_n(A)$ cancel out each other, consequently, $\bar{v}_n(E)$ reproduces the reported data. In terms of the rate of increase in $\bar{v}_n(E)$, it almost reproduces that of experimental and evaluated data, while the rate is different between the range

from 0 to 1 MeV and that from 1 to 5 MeV. As previously discussed in (2) above, it is crucial to acknowledge that the calculation conditions significantly impact $\bar{\nu}_n$. The slope also changes in the balance of the conditions; thus, we need to take into account several input conditions more carefully.

Figure 7 shows the calculated prompt fission neutron spectrum (PFNS) in the laboratory frame, and the inset is that of a ratio to a Maxwellian spectrum. Although the calculated PFNS underestimates the evaluated data from 3 MeV up to 10 MeV, the calculated one approximately reproduces the shape of the evaluated ones on a logarithmic scale. The PFNS is influenced by the spin-parity distributions of fission fragments [50,62], and it is known that the fission fragment yield also affects the tail of the PFNS [62]. It is necessary to determine the fission fragment yield and the spin-parity distribution while keeping the accuracy of other fission observables, such as the neutron multiplicity and the independent fission product



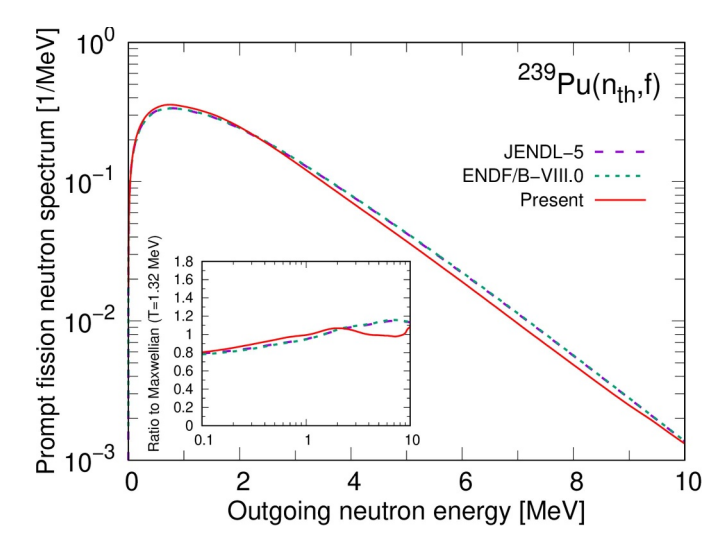


Figure 7. The calculated prompt fission neutron spectrum (PFNS) in the laboratory frame for 239 Pu(n_{th} , f). The inset figure represents the PFNS as a ratio to a Maxwellian spectrum at T = 1.32 MeV.

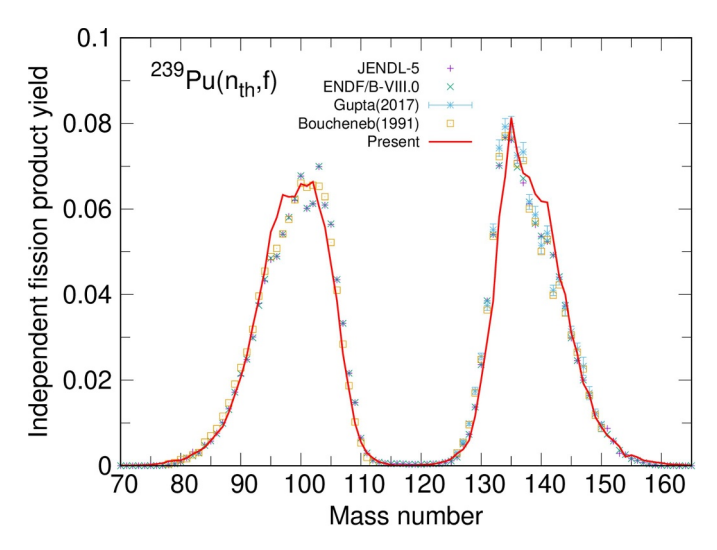


Figure 8. Comparison of the calculated independent fission product yield Y(A) with the experimental and evaluated data for $^{239}Pu(n_{th},f). \\$

yield. We have not found the solution for it, and the investigation for the PFNS and other fission observables is in progress.

Figure 8 represents the independent fission product yield Y(A) for ²³⁹Pu(n, f) at thermal energy. The accuracy of Y(A) has improved from the previous research [43] by employing two Langevin calculations of ST1 and ST2 modes. While the current approach partially reproduces fine structure in Y(A), the peak positions are slightly out by a few mass numbers compared to the experimental and evaluated data. The calculated Y(A) is overestimated in the vicinity of A = 97 for the light fragment and A = 141 for

the heavy fragment. The overestimations in Y(A)are derived from the overestimations in the fission $Y_{\rm ff}(A)$ in the vicinity of fragment yield A = 137,140. The calculation suggests that an accurate fission fragment yield $Y_{\rm ff}(A)$ is necessary to obtain an accurate independent fission product yield Y(A).

Figure 9 illustrates the independent fission product yields Y(Z,A) at the thermal energy as functions of charge and mass numbers. investigation focused on specific isotopes and revealed a notable discrepancy in Pd isotopes compared to the evaluated data. This discrepancy arises from the fact that the determination of $Y_{\rm ff}(A)$ relies

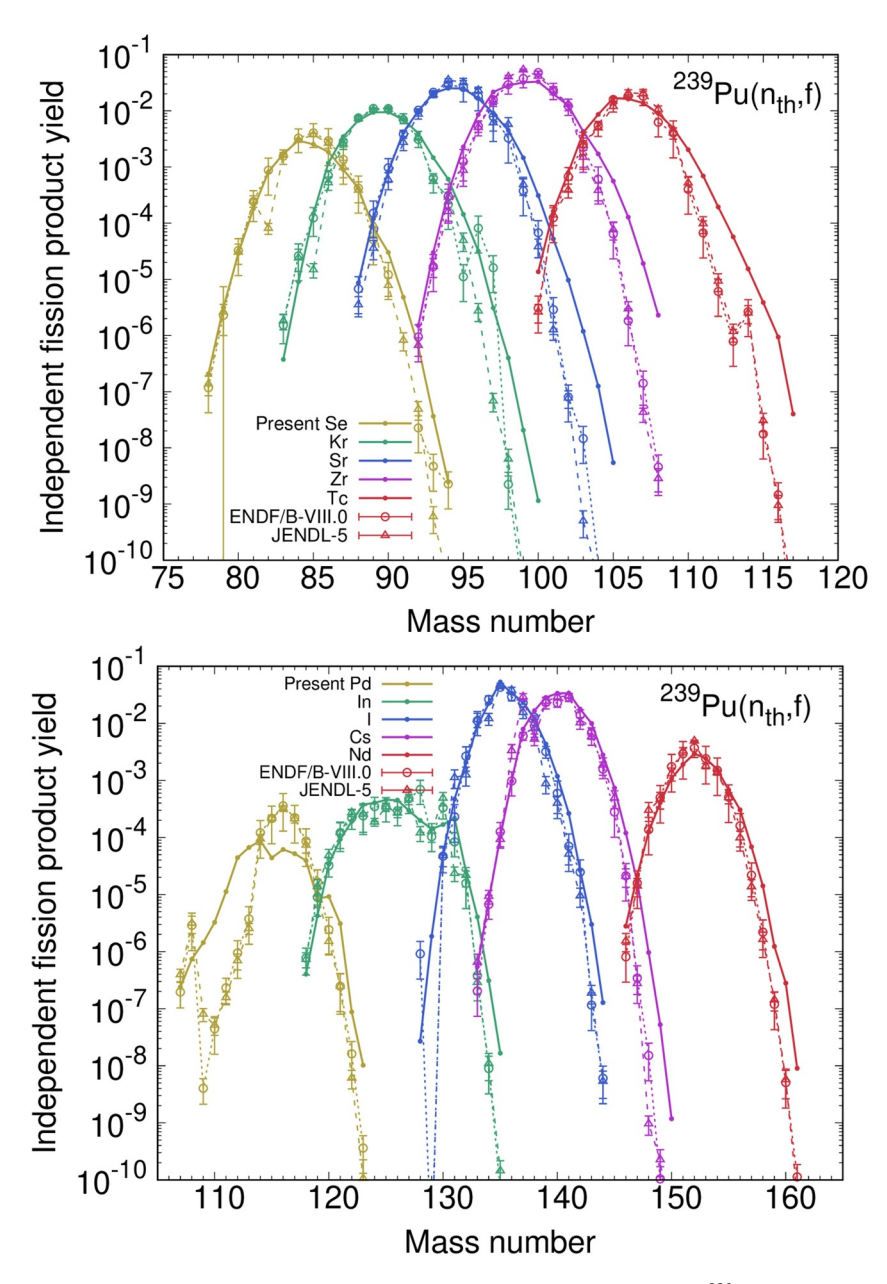


Figure 9. The calculated independent fission product yield Y(Z,A) for several isotopes of 239 Pu(n_{th} , f).

on a least squares method, and the small amount of $Y_{\rm ff}(A)$ in the symmetric region has not been adjusted reproduce the known data. to Consequently, these results emphasize the necessity of modifications within the symmetric region to enhance the accuracy of both Y(Z, A) and $Y_{\rm ff}(A)$. For the other isotopes, the calculated Y(Z,A) exhibits good agreement with the evaluated data on the lighter side. However, we can see the overestimations in Y(Z,A) on the heavier side, that is, the neutron-rich side. To further investigate this phenomenon, we investigated the charge distribution of Y(Z,A) at specific mass numbers, namely A =100, 103, 134, corresponding to the characteristic peaks in the evaluated Y(A).

Figure 10 shows the calculated Y(Z,A) as a function of charge number Z at A=100,103,134. While each Y(Z,A) shows a decent agreement with reported data on the heavier charge number side, the results are overestimated on the lighter charge number side. The lighter charge number side at the same A corresponds to neutron-rich fragments. We can conclude that Y(Z,A) calculated in our approach tends to overestimate Y(Z,A) on the neutron-rich fragments by using the original Wahl's Z_p model for 239 Pu($n_{\rm th}$, f). The neutron-richness of fission products exerts a significant influence on the neutron emission by β^- decay, thus an accurate evaluation is necessary. It clarified the necessity of adjusting the width parameters of the charge distribution to be in good agreement with the evaluated data of Y(Z,A).

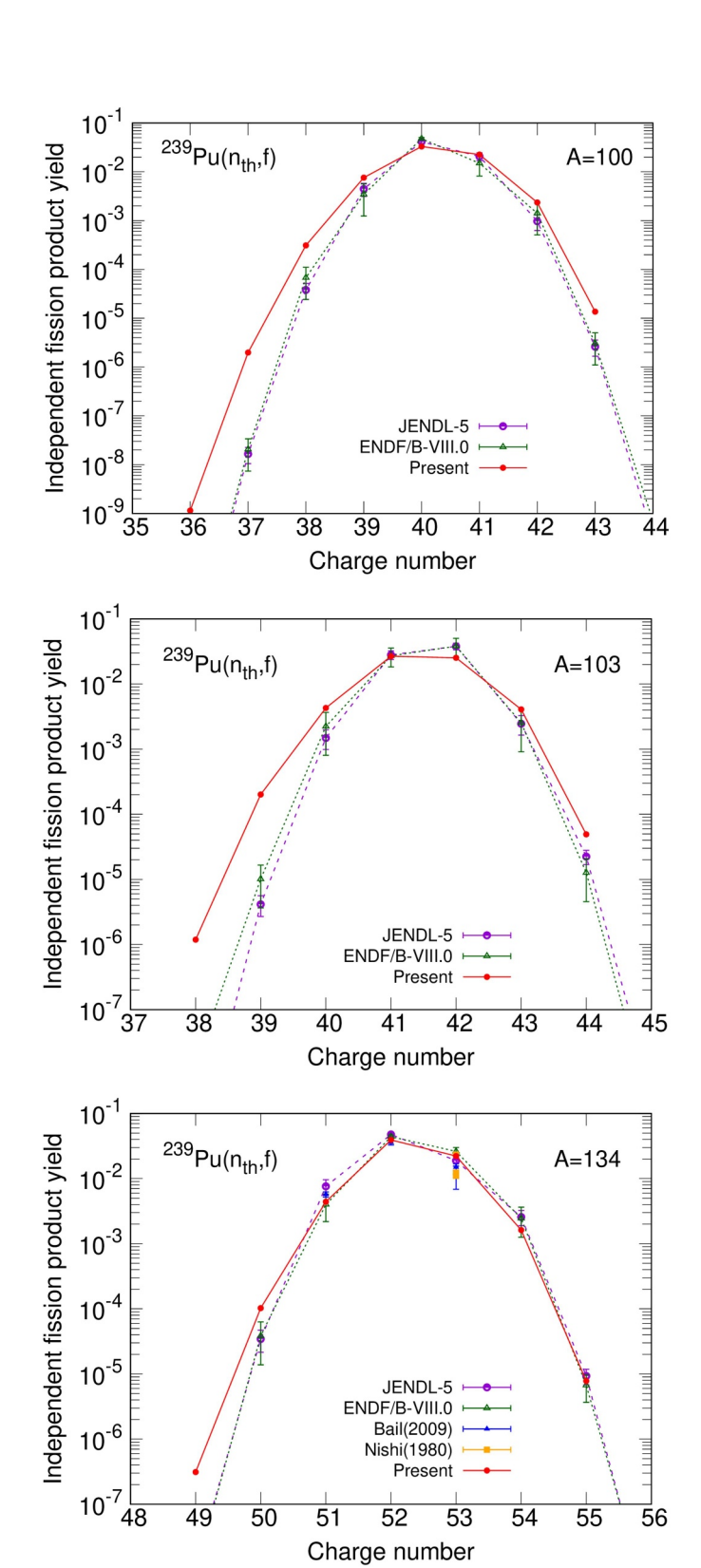


Figure 10. Comparisons of the calculated independent fission product yield Y(Z,A) with the experimental and evaluated data at A = 100, 103, 134 for ²³⁹Pu(n_{th}, f).

4. Conclusions

In this study, we established a method to simulate the fission process after forming a compound nucleus up to the prompt decay by connecting the four-dimensional Langevin model and the Hauser-Feshbach decay model. We calculated the mass distributions of the standard I and II modes separately by using the four-dimensional Langevin model and superposed them to reproduce $Y_{\rm ff}(A)$ data of $^{238,240,242}{\rm Pu}({\rm sf})$ and $^{239}{\rm Pu}({\rm n,f})$. The standard I and II modes were determined by employing different neck parameters ε within the two-center shell model shape parametrization and the zeropoint energies $\hbar\omega_u$. A systematics of the

superposing ratio ζ was found in 238,240,242 Pu(sf). In the systematics, ζ was proportional to (N-Z)/A of the fissioning nuclei, and it showed the capability to calculate $Y_{\rm ff}(A)$ and TKE for other nuclides. The superposition results reproduced the peak positions of $Y_{\rm ff}(A)$ for $^{238,240,242}{\rm Pu}({\rm sf})$ and $^{239}{\rm Pu}({\rm n,f})$. The results also reproduced the incident energy dependence of $Y_{\rm ff}(A)$ and the decreasing trend in $\langle TKE \rangle$ for $^{239}Pu(n,f)$. However, the Langevin calculations included discrepancies when compared to the known data, such as the overestimations of $Y_{\rm ff}(A)$ and the underestimations of TKE. These discrepancies have significant impacts on the prompt fission observables. Therefore, further improvements are necessary for $Y_{\rm ff}(A)$ and TKE.

Regarding the prompt fission observables of ²³⁹Pu(n, f), it was found that the calculated neutron multiplicity $\bar{\nu}_n(A)$ reproduced the saw-tooth shape and the energy dependence in $\bar{\nu}_n(A)$ while the present result has discrepancies between the experimental results in light and heavy fragments. The calculated $\bar{\nu}_n(E)$ was also in good agreement with experimental and evaluated data in the range of thermal up to 5 MeV by using the same R_T value as Ref [49]. The calculated prompt fission neutron spectrum has a discrepancy between the evaluated data, and this discrepancy is considered correlated with the spin-parity distribution of fission fragments and $Y_{\rm ff}(A)$. The independent fission yield Y(A) showed the overestimations derived from $Y_{\rm ff}(A)$. It was found that the accurate $Y_{\rm ff}(A)$ is necessary for the calculation of Y(A). The calculated Y(Z,A) were compared with experimental and evaluated data, and slight overestimations were seen on the neutron-rich side. It was found that this is attributable to a problem of the charge distribution, which was too broad, obtained by Wahl's Z_p model.

Since the prompt fission observables are all correlated, it is difficult to determine the inputs, such as the $Y_{\rm ff}(A)$, TKE, the spin-parity distribution, the energy partition, and the charge distribution. Further research is currently underway to evaluate the fission observables with high accuracy. Although challenges remain for the most important nuclides, our approach can be useful and accurate enough to provide evaluated data for other nuclides.

Acknowledgements

Authors acknowledge the Grant-in-Aid for Scientific Research (B), MEXT, Japan, and by Japan Society for the Promotion of Science (JSPS) KAKENHI Grant Number [21H01856].

Disclosure statement

No potential conflict of interest was reported by the authors.

Funding

The work was supported by the Japan Society for the Promotion of Science [21H01856].

ORCID

Kazuki Fujio (b) http://orcid.org/0009-0006-0798-4470 Shin Okumura http://orcid.org/0000-0001-5964-3615 Chikako Ishizuka (D) http://orcid.org/0000-0002-1046-1658 Satoshi Chiba http://orcid.org/0000-0001-7123-7230 Tatsuya Katabuchi http://orcid.org/0000-0002-1686-4570

References

- [1] Tsujimoto K, Oigawa H, Ouchi N, et al. Research and development program on accelerator driven subcritical system in JAEA. J Nucl Sci Technol. 2007;44 (3):483–490. doi: 10.1080/18811248.2007.9711312
- [2] Mukaiyama T, Takizuka T, Mizumoto M, et al. Review of research and development of accelerator driven system in Japan for transmutation of long-lived nuclides. Prog Nucl Energy. 2001;38 (1):107134. Accelerator Transmutation of Waste. doi: 10.1016/S0149-1970(00)00098-6
- [3] Chiba S, Wakabayashi T, Tachi Y, et al. Method to reduce long-lived fission products by nuclear transmutations with fast spectrum reactors. Sci Rep. 2017 Oct;7(1):13961. doi: 10.1038/s41598-017-14319-7
- [4] Wahl AC. Nuclear-charge distribution delayed-neutron yields for thermal-neutron-induced fission of ²³⁵U, ²³³U and ²³⁹Pu and for spontaneous fission of ²⁵²Cf. At Data Nucl Data Tables. 1988;39(1):1-156.
- [5] Wahl AC. Systematics of fission-product yields. Los Alamos Nat Lab. 2002;LA-13928.
- [6] Katakura JI. A systematics of fission product mass yields with 5 Gaussian functions. Japan At Energy Res Inst. 2003;2003-004.
- [7] Madland DG, Nix JR. New calculation of prompt fission neutron spectra and average prompt neutron multiplicities. Nucl Sci Eng. 1982;81(2):213-271. doi: 10.13182/NSE82-5
- [8] Lemaire S, Talou P, Kawano T, et al. Monte Carlo approach to sequential neutron emission from fission fragments. Phys Rev C. 2005 Aug;72(2):024601. doi: 10.1103/PhysRevC.72.024601
- [9] Talou P, Stetcu I, Jaffke P, et al. Fission fragment decay simulations with the CGMF code. Comput Phys Commun. 2021;269:108087. doi: 10.1016/j.cpc. 2021.108087
- [10] Litaize O, Serot O. Investigation of phenomenological models for the Monte Carlo simulation of the prompt fission neutron and γ emission. Phys Rev C. 2010 Nov;82(5):054616. doi: 10.1103/PhysRevC.82.054616
- [11] Randrup J, Vogt R. Calculation of fission observables through event-by-event simulation. Phys Rev C. 2009 Aug;80(2):024601. doi: 10.1103/PhysRevC.80.024601
- [12] Vogt R, Randrup J, Pruet J, et al. Event-by-event study of prompt neutrons from ²³⁹Pu(n,f). Phys Rev C. 2009 Oct;80(4):044611.
- Schmidt KH, Jurado B, Amouroux C, et al. General description of fission observables: GEF model code. Nucl Data Sheets Special Issue on Nuclear Reaction Data. 2016;131:107-221. doi: 10.1016/j.nds.2015.12.009



- [14] Tudora A, Hambsch FJ, Tobosaru V. Revisiting the residual temperature distribution in prompt neutron emission in fission. Eur Phys J A. 2018 May;54(5):87. doi: 10.1140/epja/i2018-12521-7
- [15] Okumura S, Kawano T, Jaffke P, et al. ²³⁵U(n,f) independent fission product yield and isomeric ratio calculated with the statistical Hauser-Feshbach theory. J Nucl Sci Technol. 2018;55(9):1009-1023.
- [16] Tudora A. Experimental prompt fission neutron "sawtooth" data described by the "point by point" model. Ann Nucl Energy. 2006;33(11):1030-1038. doi: 10.1016/j.anucene.2006.04.007
- [17] Koning A, Rochman D. Modern nuclear data evaluation with the TALYS code system. Nucl Data Sheets. 2012;113(12):2841-2934. Special Issue on Nuclear Reaction Data. doi: 10.1016/j.nds.2012.11.002
- [18] Sadhukhan J, Nazarewicz W, Schunck N. Microscopic modeling of mass and charge distributions in the spontaneous fission of ²⁴⁰Pu. Phys Rev C. 2016 Jan;93(1):011304. doi: 10.1103/PhysRevC.93.011304
- [19] Tanimura Y, Lacroix D, Ayik S. Microscopic Phase-Space Exploration Modeling of 258Fm spontaneous fission. Phys Rev Lett. 2017 Apr;118 (15):152501. doi: 10.1103/PhysRevLett.118.152501
- [20] Lemaître JF, Goriely S, Hilaire S, et al. Fully microscopic scission-point model to predict fission fragment observables. Phys Rev C. 2019 Mar;99 (3):034612. doi: 10.1103/PhysRevC.99.034612
- [21] Bulgac A, Jin S, Roche KJ, et al. Fission dynamics of ²⁴⁰Pu from saddle to scission and beyond. Phys Rev C. 2019 Sep;100(3):034615. doi: 10.1103/PhysRevC.100. 034615
- [22] Bulgac A, Jin S, Stetcu I. Nuclear fission dynamics: past, present, needs, and future. Front Phys. 2020;8. doi: 10.3389/fphy.2020.00063
- [23] Zhao K, He Y, Li Z, et al. The description of dynamical fission process using improved quantum molecular dynamics model incorporated with microscopic surface. Phys potential energy Lett 2023;839:137817. doi: 10.1016/j.physletb.2023.137817
- [24] Asano T, Wada T, Ohta M, et al. Dynamical calculation of multi-modal nuclear fission of fermium nuclei. J Nucl Radiochem Sci. 2004;5(1):1-5. doi: 10. 14494/jnrs2000.5.1
- [25] Randrup J, Möller P. Brownian shape motion on five-dimensional potential-energy surfaces: nuclear fission-fragment mass distributions. Phys Rev Lett. 2011 Mar;106(13):132503. doi: 10.1103/PhysRevLett. 106.132503
- [26] Aritomo Y, Chiba S, Ivanyuk F. Fission dynamics at low excitation energy. Phys Rev C. 2014 Nov;90 (5):054609. doi: 10.1103/PhysRevC.90.054609
- [27] Pasca H, Andreev A, Adamian G, et al. Possible origin of transition from symmetric to asymmetric fission. Phys Lett B. 2016;760:800-806. doi: 10.1016/j.phy sletb.2016.07.074
- [28] Sierk AJ. Langevin model of low-energy fission. Phys Rev C. 2017 Sep;96(3):034603. doi: 10.1103/ PhysRevC.96.034603
- [29] Ishizuka C, Usang MD, Ivanyuk FA, et al. Fourdimensional Langevin approach to low-energy nuclear fission of ²³⁶U. Phys Rev C. 2017 Dec;96 (6):064616. doi: 10.1103/PhysRevC.96.064616
- [30] Jaffke P, Möller P, Talou P, et al. Hauser-Feshbach fission fragment de-excitation with calculated macroscopic-microscopic mass yields.

- Phys Rev C. 2018 Mar;97(3):034608. doi: 10. 1103/PhysRevC.97.034608
- [31] Carjan N, Ivanyuk FA, Oganessian YT. Fission of superheavy nuclei: fragment mass distributions and their dependence on excitation energy. Phys Rev C. 2019 Jun;99(6):064606. doi: 10.1103/PhysRevC.99.064606
- Mumpower MR, Jaffke P, Verriere M, et al. Primary fission fragment mass yields across the chart of nuclides. Phys Rev C. 2020 May;101(5):054607. doi: 10.1103/PhysRevC.101.054607
- Usang MD, Ivanyuk FA, Ishizuka C, et al. Correlated transitions in TKE and mass distributions of fission fragments described by 4-D Langevin equation. Sci Rep. 2019 Feb;9(1):1525. doi: 10.1038/s41598-018-37993-7
- [34] Ishizuka C, Zhang X, Usang MD, et al. Effect of the doubly magic shell closures in 132Sn and 208Pb on the mass distributions of fission fragments of superheavy nuclei. Phys Rev C. 2020 Jan;101(1):011601. doi: 10. 1103/PhysRevC.101.011601
- [35] Maruhn J, Greiner W. The asymmetric two center shell model. Z Phys. 1972 Oct;251(5):431-457. doi: 10.1007/BF01391737
- [36] Ivanyuk FA, Ishizuka C, Usang MD, et al. Temperature dependence of shell corrections. Phys Rev C. 2018 May;97(5):054331. doi: 10.1103/ PhysRevC.97.054331
- [37] Pashkevich V. On the asymmetric deformation of fissioning nuclei. Nucl Phys A. 1971;169(2):275293. doi: 10.1016/0375-9474(71)90884-0
- [38] Kelson I. Dynamic calculations of fission of an axially symmetric liquid drop. Phys Rev. 1964 Dec;136(6B): B1667-B1673. doi: 10.1103/PhysRev.136.B1667
- [39] Davies KTR, Sierk AJ, Nix JR. Effect of viscosity on the dynamics of fission. Phys Rev C. 1976 Jun;13 (6):2385-2403. doi: 10.1103/PhysRevC.13.2385
- [40] Blocki J, Boneh Y, Nix J, et al. One-body dissipation and the super-viscidity of nuclei. Ann Phys. 1978;113 (2):330–386. doi: 10.1016/0003-4916(78)90208-7
- [41] Sierk AJ, Nix JR. Fission in a wall-and-window one-body-dissipation model. Phys Rev C. 1980 Mar;21(3):982-987. doi: 10.1103/PhysRevC.21.982
- [42] Adeev G, Karpov A, Nadtochy P, et al. Multidimensional stochastic approach to fission dynamic of excited nuclei. Phys Part Nucl. 2005 07;36(4):378-426.
- [43] Okumura S, Kawano T, Chiba S. The fission yield calculations with Langevin model, HauserFeshbach statistical decay, and beta decay. EPJ Web Conf. 2020;239:03005. doi: 10.1051/epjconf/202023903005
- [44] Brosa U, Grossmann S, Muller A. Nuclear scission. Phys Rep. 1990;197(4):167–262. doi: 10.1016/0370-1573(90)90114-H
- [45] Schillebeeckx P, Wagemans C, Deruytter A, et al. Comparative study of the fragments' mass and energy characteristics in the spontaneous fussion of ²³⁸Pu, ²⁴⁰Pu and ²⁴²Pu and in the thermal neutron-induced fission of ²³⁹Pu. Nucl Phys A. 1992;545(3):623–645.
- [46] Ohsawa T, Horiguchi T, Hayashi H. Multimodal analysis of prompt neutron spectra for ²³⁷Np(n,f). Nucl Phys A. 1999;653(1):17-26. doi: 10.1016/ S0375-9474(99)00156-6
- [47] Ohsawa T, Horiguchi T, Mitsuhashi M. Multimodal analysis of prompt neutron spectra for ²³⁸Pu(sf), 240 Pu(sf), 242 Pu(sf) and 239 Pu(n_{th} ,f). Nucl Phys A. 2000;665(1):3-12. doi: 10.1016/S0375-9474(99)00686-7



- [48] Kawano T, Talou P, Stetcu I, et al. Statistical and evaporation models for the neutron emission energy spectrum in the center-of-mass system from fission fragments. Nucl Phys A. 2013;913(2):51-70. doi: 10. 1016/j.nuclphysa.2013.05.020
- [49] Okumura S, Kawano T, Lovell AE, et al. Energy dependent calculations of fission product, prompt, and delayed neutron yields for neutron induced fission on ²³⁵U, ²³⁸U, and ²³⁹Pu. J Nucl Sci Technol. 2022;59 (1):96-109. doi: 10.1080/00223131.2021.1954103
- Fujio K, Al-Adili A, Nordström F, et al. TALYS calculations of prompt fission observables and independent fission product yields for the neutron-induced fission of ²³⁵U. Eur Phys J A. 2023 Aug;59(8):178. doi: 10.1140/epja/s10050-023-01095-4
- [51] Dematte L, Wagemans C, Barthelemy R, et al. Fragments' mass and energy characteristics in the spontaneous fission of ²³⁶Pu, ²³⁸Pu, ²⁴⁰Pu, ²⁴²Pu, and ²⁴⁴Pu. Nucl Phys A. 1997;617(3):331–346. doi: 10. 1016/S0375-9474(97)00032-8
- [52] Wagemans C. Contemporary fission. Proc 5th Int Symp On Nucleon Induced Reactions. 1988;15:286-304.
- [53] Wagemans C. On the necessity of alternative methods to determine sample thicknesses and masses. Nucl Instrum Methods Phys Res A. 1989;282(1):4-9. doi: 10.1016/0168-9002(89)90102-2
- [54] Surin VM, Sergachev AI, Rezchikov NI, et al. Yields and kinetic energies of fragments at the fission of $^{233}\mathrm{U}$ and $^{239}\mathrm{Pu}$ by 5.5 and 15MeV neutrons. Yadern Fiz. 1971 Nov;14(5):935-938.
- [55] Tsuchiya C, Nakagome Y, Yamana H, et al. Simultaneous measurement of prompt neutrons and

- fission fragments for ²³⁹Pu(n_{th},f). J Nucl Sci Technol. 2000;37(11):941-948. doi: 10.1080/18811248.2000. 9714976
- [56] Shimada K, Ishizuka C, Ivanyuk FA, et al. Dependence of total kinetic energy of fission fragments on the excitation energy of fissioning systems. Phys Rev C. 2021 Nov;104(5):054609. doi: 10.1103/ PhysRevC.104.054609
- Müller R, Naqvi AA, Käppeler F, et al. Fragment velocities, energies, and masses from fast neutron induced fission of ²³⁵U. Phys Rev C. 1984 Mar;29 (3):885-905. doi: 10.1103/PhysRevC.29.885
- Naqvi AA, Käppeler F, Dickmann F, et al. Fission fragment properties in fast-neutron-induced fission of ²³⁷Np. Phys Rev C. 1986 Jul;34:218–225.
- Tudora A, Hambsch FJ, Visan I, et al. Comparing different energy partitions at scission used in prompt emission model codes GEF and point-by-point. Nucl Phys A. 2015;940:242-263. doi: 10.1016/j.nuclphysa. 2015.04.012
- [60] Thulliez L, Litaize O, Serot O, et al. Neutron and γ multiplicities as a function of incident neutron energy for the ²³⁷Np(n,f) reaction. Phys Rev C. 2019 Oct;100:044616.
- [61] Tudora A. Influence of energy partition in fission and pre-neutron fragment distributions on postneutron fragment yields, application for ²³⁵U(n_{th},f). Eur Phys J A. 2022 Jul;58(7):126. doi: 10.1140/epja/s10050-022-00766-у
- [62] Kawano T, Okumura S, Lovell AE, et al. Influence of nonstatistical properties in nuclear structure on emission of prompt fission neutrons. Phys Rev C. 2021 Jul;104(1):014611. doi: 10.1103/PhysRevC.104.014611